

A MATHEMATICAL MODEL FOR FORCE GENERATION AT THE KINETOCHORE-MICROTUBULE INTERFACE*

BLERTA SHTYLLA[†] AND JAMES P. KEENER[†]

Abstract. In this paper we construct and analyze a mathematical model for kinetochore (Kt) motors operating at the chromosome/microtubule interface. Motor dynamics are modeled using a jump-diffusion process that incorporates biased diffusion due to the binding of microtubules (MTs) by Kt binder elements and thermal ratchet forces that arise when the polymer grows against the Kt plate. The resulting force-velocity relationships are nonlinear and depend on the strength of MT binding at Kts, as well as the spatial distribution of binders and of MT rate-altering enzymes inside the Kt. In the case when Kt binders are weakly bound and spaced with the same period as the MT binding sites, the numerical results for the motor force-velocity relation and breaking loads are in complete agreement with our approximate analytic solutions. We show that in this limit motor velocity depends directly on the balance of polymer tip polymerization/depolymerization rates and is fairly insensitive to load variations. In the strong binding regime, the motor can support attachment for large Kt loads but responds with smaller velocities, independent of the polymer tip dynamics. When the Kt binders are redistributed with spacing off-register from the MT lattice period, our numerics match our analytical velocity results independent of binding strength at Kts; motor velocities do not decrease in response to binding strength variation in this case.

Key words. kinetochore coupler motor, jump-diffusion process, force-velocity relationship

AMS subject classification. 92C05

DOI. 10.1137/100802645

1. Introduction. Molecular motor enzymes that harvest the chemical energy of adenosine triphosphate (ATP) hydrolysis to move unidirectionally are used in various cellular processes. However, cells sometimes make use of mechanisms for motion that do not involve ATP-dependent molecular motors. Cellular protrusions such as filopodia and lamellipodia, for example, do not appear to involve molecular motors but instead use thermal ratchets in conjunction with dynamic polymers to generate motion [13]. Another example comes from mitosis, where chromosomes move by tethering to the dynamic tips of microtubules (MTs) in an ATP-independent fashion [1], [4]. The mechanisms underlying this dynamic coupling of chromosome movement to attached polymerizing/depolymerizing MTs is not well understood.

A chromosome moves by attaching to MT plus ends with the help of specialized macromolecular complexes called Kts. For each chromosome arm, a single Kt complex that can bind either one or several MTs at once is assembled on the chromatid. MTs are hollow cylindrical structures that contain 13 linear protofilaments composed of α - β tubulin dimers. During mitosis MTs stochastically transition between growth and shortening states both when they are attached (kMTs) or not attached to a kinetochore [1]. For a polymerizing MT, guanosine triphosphate (GTP)-tubulin is added at the growing end; these dimers have a preferred flat orientation relative to the polymer lattice. Subsequently, GTP-tubulin is hydrolyzed with some time delay into guanosine diphosphate (GDP)-tubulin, which prefers a bent conformation. Inside the lattice, lateral tubulin interactions hold the monomers in a straight conformation

*Received by the editors July 19, 2010; accepted for publication (in revised form) June 27, 2011; published electronically October 11, 2011. This research was supported in part by NSF grant DMS-0718036.

<http://www.siam.org/journals/siap/71-5/80264.html>

[†]Mathematics Department, University of Utah, Salt Lake City, UT 84112 (shtyllab@math.utah.edu, keener@math.utah.edu).

with the energy of hydrolysis stored as strain. When the lateral interactions are lost, the strain is released so that the ends of depolymerizing MT protofilaments bend and the MT tips become gently flared.

Two important motility characteristics of chromosome movement have been observed experimentally. First, chromosome movement has been shown to be coupled to the polymerization/depolymerization state of an inserted MT [10] with velocities dependent on the balance of kMT tip polymerization/depolymerization rates. Second, Kts that are attached to a spindle pole by tethering to a kMT display toward and away motion with similar speeds [16] indicating that Kt motors are fairly insensitive to variations in load.

Several theoretical models that propose various force-generation mechanisms at Kts have been put forward. These models can be separated into two distinct classes: (1) biased diffusion models, and (2) forced walk models. Each model uses variations in Kt motor (coupler) geometry and size to convert the energy of Kt-MT interactions into useful work [7].

The first model for chromosome attachment, initially advanced by Hill [5], uses a biased diffusion mechanism. Hill's model proposes that movement is facilitated by a rigid array (so-called sleeve) of weak binding sites that diffuse on the lattice of a kMT. An increased overlap between the sleeve and the lattice is favorable due to free energy decrease from the attachment of more bonds between the sleeve coupler and the MT. As the MT shortens, sleeve diffusion relocates the bonds so that overlap is preserved, generating poleward motion, i.e., biased diffusion. The key aspects of this model are that it allows for continuous attachment for both growing and shortening MTs, and also produces speeds that are fairly insensitive to load, in good agreement with experimental data.

Forced walk models use the force of flaring of depolymerizing MT tips in conjunction with force couplers (such as rings) built to resist protofilament outward bending in order to generate depolymerization-coupled movement [11]. If constructed appropriately, these motors can track depolymerizing tips efficiently. However, attachment cannot be maintained when a polymer transitions into a polymerizing state (with blunt ends), nor do velocities remain constant for varying loads. Therefore these types of motors fail to capture the full range of chromosome motions seen experimentally.

Recent experiments indicate that binding at Kts is weak and that diffusion may play a significant role in movement [14], [17]. These results seem to support a biased diffusion mechanism but also provide new data that require a more comprehensive treatment of the biased diffusion mechanism at play. Hill's model uses a discrete Markov chain model to show that attachment can be maintained at steady state for a Kt attached to a slowly depolymerizing tip. This work was extended by [6] to account for polymer growth inside the sleeve. In both cases, the transition rate assumptions are valid only in the high activation barrier limit, and model implementation into a larger scale mitosis model requires time consuming numerical simulations. Furthermore, for the biased diffusion models that have been studied thus far there has been no inclusion of polymerization thermal ratchet effects that arise when the inserted kMT grows against the Kt plate. Also, to our knowledge, the biased diffusion model has not been studied when there are variations in the spatial distributions of Kt binders on the MT lattice.

The present paper is aimed at developing a mathematical model for Kt motors that incorporates a biased diffusion mechanism but also takes into account several features of Kt motors not addressed in previous biased diffusion models. This paper is organized as follows. In section 2 we state model assumptions and derive model

equations. Then we separate our study into two parts. In the first part of the paper (sections 3 and 4) we consider the case when the spacing between the Kt binders and the MT lattice binding sites are integer multiples of each other (in-register case); in the second part (sections 5 and 6) we examine the case when binder spacing is not an integer multiple of the MT lattice binding site spacing (off-register case). In section 3 we find numerical solutions for system breaking loads and the force-velocity relation when the strength of binding between the motor and the MT lattice is varied. In section 4 we use homogenization to find analytical expressions for the breaking loads and the force-velocity relation in the limit of low unit activation energy for binding. Finally, in sections 5 and 6 we repeat our simulations and calculations from sections 3 and 4 for the off-register case.

2. Mathematical model. Based on recent structural data [1], [9], it is assumed that a Kt motor consists of a collection of fibers extending from the Kt plate, each with multiple binding attachments (motor binders) that can weakly bind onto the lattice of an inserted MT; see Figure 2.1. These fibers form a structure analogous to the rigid sleeve of Hill, but they are assumed to be sufficiently flexible so that they can attach to the flaring MTs. The MT lattice is assumed to have one motor binder binding site per tubulin dimer. Thus, each binder has an additional preference to attach to a specific binding site after associating with the MT lattice.

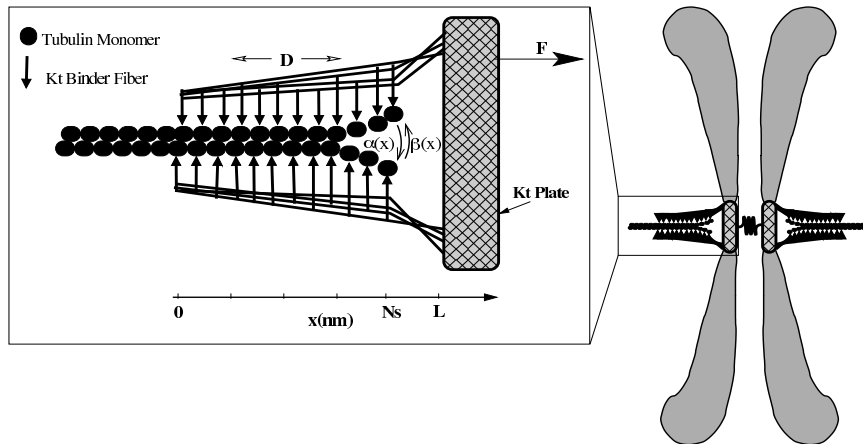


FIG. 2.1. A schematic of the Kt motor model components. The Kt is composed of several binder fibers which are connected to the Kt plate on one end and can bind the MT lattice. For a Kt motor, N binders are uniformly spaced a distance s apart from one another along the MT lattice, from $x = 0$ to $x = Ns$. The attached MT polymer is dynamic, and the tip polymerizes/depolymerizes with prescribed rates $\alpha(x), \beta(x)$.

Since a motor binder is assumed to be weakly bound to an MT, the Kt binders experience thermal motion (diffusion) on the lattice of an attached MT. However, since the binders are physically linked to each other on the fibers, the entire coupler experiences one-dimensional diffusion on the polymer lattice.

Finally, a polymer embedded in the Kt motor can grow/shorten with prescribed polymerization/depolymerization rates, specified below. We also assume that if due to thermal motion the Kt plate is pushed against the polymer tip, polymerization is prevented by the lack of space, while the energy of polymerization is sufficiently large so that a tubulin monomer is not subsequently cleaved [13].

To describe the motion of the Kt motor, we suppose that motion is one-dimensional along the horizontal x -axis. The motor position variable, x , marks the distance between the polymer tip and the coupler end distal to the Kt plate. Thus, the position axis starts at the coupler entry point ($x = 0$ nm) and extends to the Kt plate ($x = L$); see Figure 2.1.

In the viscous-dominated limit, the motor system can be modeled with a one-dimensional jump-diffusion process described by the stochastic differential equation (Langevin equation)

$$(2.1) \quad dx(t) = \frac{1}{\nu}(-\Psi'(x) - F)dt + \sigma_D(x(t))dW_t + \delta dN_\alpha(t) + \delta dN_\beta(t),$$

where $x(t)$ represents the position of the polymer tip relative to the coupler; $N_\alpha(t)$ and $N_\beta(t)$ are independent homogenous Poisson processes with amplitudes δ (tubulin size) and position dependent rates $\alpha(x)$ and $\beta(x)$, which govern MT tubulin addition/removal, respectively; and W_t is standard white noise applied to the motor with amplitude $\sigma_D(x(t))$. The term $\Psi'(x)$ represents polymer lattice binding forces, F describes loads on the Kt motor, and ν is the effective drag coefficient for the coupler.

Binding interactions between the coupler and the polymer are characterized by the potential function, $\Psi(x)$. We construct this function by envisioning the MT polymer as a semi-infinite linear chain of monomer beads that are rigidly connected. For an MT with 13 protofilaments and 8 nm long tubulin dimers, the monomer size in the linear chain is $\delta = 8/13$ nm. Individual binders can attach to the monomer beads with potential energy function $\psi(x)$, as shown in Figure 2.2. The net energy associated with polymer binding by the motor is the sum of the potential energy of all attached binders,

$$(2.2) \quad \Psi(x) = \sum_{n=0}^N \psi(x - ns).$$

The unit energy terms $\psi(x)$ in the sum are shifted by an arbitrary amount s to account for the offset between consecutive Kt binders. We use

$$(2.3) \quad \psi(x) = \frac{b}{2} \sin\left(\frac{2\pi x}{\delta}\right) \left(1 + \tanh(\lambda_1 x)\right) - \frac{a}{2} \left(1 + \tanh(\lambda_2 x)\right),$$

with $\lambda_1 \gg \lambda_2$. An exact representation of the function $\Psi(x)$ can be given; however, it is more convenient for computational purposes to use an approximate representation for the well, which we provide in the following sections.

In our analysis we consider two cases for the shift parameter s : (a) $s = \delta$, in which case the period of the binders is the same as the MT lattice binding site period (in-register), and (b) $s = \bar{\kappa}\delta$, where $\bar{\kappa}$ is not an integer (off-register). In the second case, we are interested in $\bar{\kappa} > 1$ since for these values the number of linkers that can bind the MT is in good agreement with the binder numbers recently predicted in experimental studies [14].

For this model binding involves two steps: first binder association with the polymer and then binder transition on the lattice due to additional preference for polymer binding sites. Therefore, for $\psi(x)$ we assume that for each new binding interaction established between the binders and the polymer, the system free energy is lowered by the amount “ $-a$ ”; see Figure 2.2. Once one binder is engaged, it then has to hop between δ separated binding sites on the MT lattice, which produces the periodic part

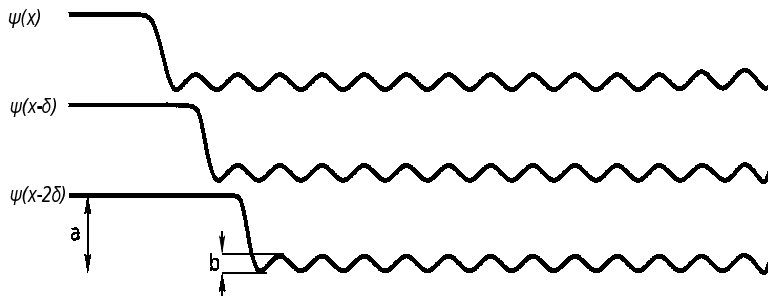


FIG. 2.2. Diagram of potential well components functions, $\psi(x)$. The energy function becomes periodic when a binder is bound to the MT due to the polymer lattice binding site periodicity.

of the unit energy function $\psi(x)$. Each thermally induced hopping event of the linkers on the polymer lattice has to overcome a unit potential energy barrier corresponding to the energy needed for existing bonds to break and a new one to reform. We denote the barrier by “b” in the well; see Figure 2.2. While the kMT increases overlap with the Kt motor, more bonds are established so that total system free energy in Ψ decreases in multiples of a ; however, more bonds must also be broken so that the net potential barrier increases by some multiple of b ; see Figure 2.3. The rate of increase in the net barrier for Ψ depends on the overlap parameter s . When $s = \delta$, the net barrier increases linearly, since for each attachment event exactly one bond must be broken to readjust the overlap. If, on the other hand, $s = \bar{\kappa}\delta$, then the net activation barrier grows more slowly than linear as overlap increases. In both cases, we obtain a corrugated well $\Psi(x)$ that has the net effect of a drift force that biases the diffusion of the polymer further inside the coupler.

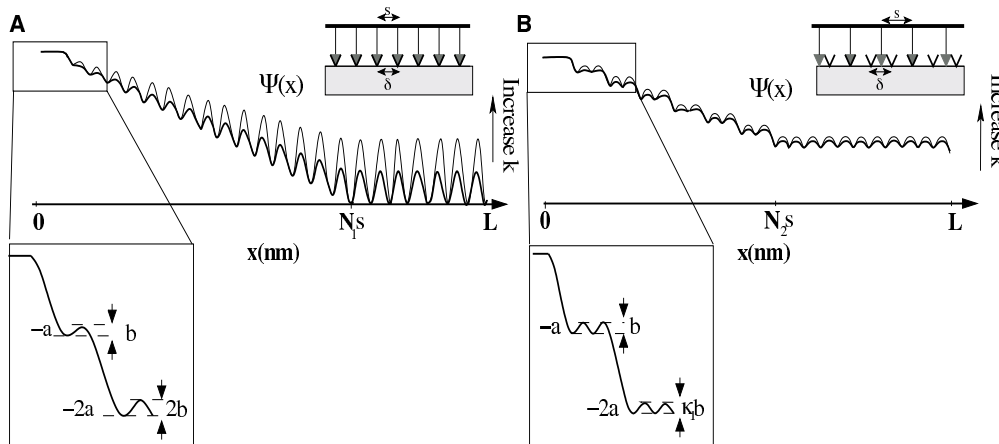


FIG. 2.3. Diagram of the potential energy well $\Psi(x)$ for varying s . (A) The potential energy well for the in-register well with binder spacing $s = \delta$. (B) The potential energy well for the off-register well with $s = \bar{\kappa}\delta$.

It is possible that the polymer tip moves either by diffusion or polymerization past the last coupler binder. At this position all the available binding sites are occupied, so there is no gain for the system to bias thermal motion in either direction; further kMT insertion into the coupler does not lower the free energy. Nonetheless, if the coupler

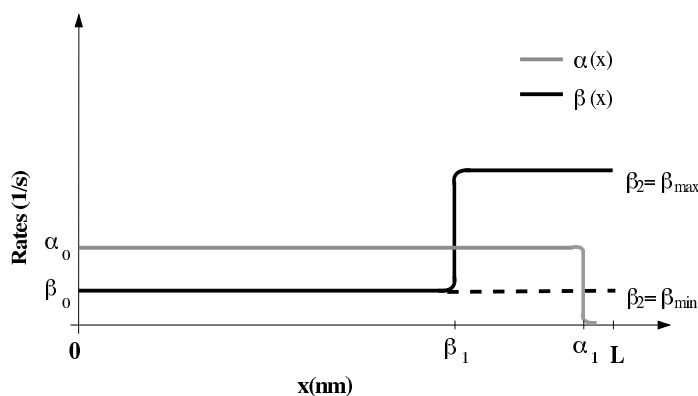


FIG. 2.4. *Kt MT tip rate functions. The polymerization rate is given by $\alpha(x)$, and $\beta(x)$ describes the depolymerization rate. Parameter values are given in Table 2.1.*

moves in this region, it must cross the potential barrier associated with breaking all N_1 or N_2 bonds. Consequently, the potential well function $\Psi(x)$ loses its tilt and becomes periodic past the last binder position at $x = N_i s$ nm as shown in Figures 2.3(A) and 2.3(B). The numbers N_1, N_2 are chosen such that the motor binders are uniformly spread along ≈ 40 nm for both the in-register and off-register Kt motors.

Spindle forces acting on a chromosome create mechanical stress on Kts, which in turn produces load, F , on the motor. With our sign convention, $F > 0$ pushes on a Kt in such a way as to increase the distance between the polymer tip and the Kt (i.e., to decrease x), whereas $F < 0$ favors polymer tip insertion toward $x = L$, increasing x .

Finally, the tip of the inserted polymer is dynamic and can grow or shorten with prescribed rates that vary with the position of the tip relative to the Kt coupler. A plot of the rates is shown in Figure 2.4. We assume that a powerful depolymerase (such as MCAK [1]) is enriched at the coupler end proximal to the Kt plate. Hence, we choose a depolymerization rate that depends on the position of the kMT tip relative to the motor with $\beta(x) = \beta_0 + \frac{\beta_2 - \beta_0}{1 + \exp(-\lambda(x - \beta_1))}$, where λ controls the steepness of the transitions and $\beta_1 < N_i s$. On the other hand, we keep the polymerization rate constant independent of the MT tip position relative to the coupler, except for the restriction that if the polymer tip is located less than δ away from the $x = L$ boundary, then no new monomers can be inserted with $\alpha(x) = \frac{\alpha_0}{1 + \exp(\lambda(x - \alpha_1))}$. We note here that we have not chosen the polymerization rate to be a Heaviside function as in [13]. This is because, we believe, it is unlikely that the polymerization rate drops instantaneously at the $x = L - \delta$ position if one takes into account random fluctuations in MT monomer size. Thus, we assume that a space slightly more than δ between the polymer tip and the KT plate is necessary for the MT to be able to polymerize at the full rate α_0 . Finally, the constant basal polymerization and depolymerization rates α_0, β_0 reflect the presence of several Kt enzymes that have been shown to favor slow kMT growth or shortening [1].

The stochastic differential equation in (2.1) corresponds to the forward Chapman–Kolmogorov equation [3]

$$(2.4) \quad \frac{\partial p(x, t)}{\partial t} = -\frac{1}{\nu} \frac{\partial}{\partial x} \left(V'(x) p(x, t) \right) + D \frac{\partial^2}{\partial x^2} p(x, t) + \alpha(x - \delta) p(x - \delta, t) \\ + \beta(x + \delta) p(x + \delta, t) - (\alpha(x) + \beta(x)) p(x, t),$$

where $p(x, t)$ is the probability density function for the relative position of the attached MT tip with respect to the coupler, x , and $V'(x) = -\Psi'(x) - F$. For the additive Gaussian noise we take $\sigma_D(x(t)) = \sqrt{2D}$, where D is the diffusion coefficient of the coupler, calculated according to the Einstein relation $D = k_B T/\nu$. The value used for this coefficient agrees with coefficients chosen in previous models [5], [6].

To complete the specification of the problem, we impose a reflecting boundary at $x = L$, where the Kt wall physically impedes polymer penetration. At $x = 0$, we prescribe an absorbing boundary, since if the polymer tip crosses this point, the coupling connection is broken and not likely to be reestablished. Unless otherwise stated, the parameters used for calculations in this paper are those in Table 2.1.

TABLE 2.1

Model parameter values. Some parameters are estimated from parameter ranges reported in the literature. The specific values chosen here produce motor velocities that are in agreement with chromosome movement velocities observed in newt lung cells [16].

Parameter	Description	Value
L	Kt thickness	50 nm [1]
δ	binding site period on the MT lattice	8/13 nm
ν	effective viscous drag coefficient	6 pNs/ μm [6]
α_0	rate of tubulin subunit addition	80 s^{-1} [6]
β_0	basal rate of tubulin subunit removal	27 s^{-1} [6]
β_2	max. rate of removal of tubulin	27 s^{-1} , 100 s^{-1} (estimated)
β_1	depol. rate transition point	35 nm (estimated)
α_1	pol. rate transition point	$L - 1.6\delta$ (estimated)
a	free energy of binding	2.6 $k_B T$ [5]
D	coupler diffusion coefficient	690 nm^2/s [5][6]
N_1	in-register Kt binder number	65
N_2	off-register Kt binder number	30

3. In-register well. We approximate the potential well function of the in-register case with

$$(3.1) \quad \Psi(x) = \begin{cases} f(x) (1 - \cos(\frac{2\pi x}{\delta})) + h(x), & x \leq N_1 \delta, \\ f(N_1 \delta) (1 - \cos(\frac{2\pi x}{\delta})) + h(N_1 \delta), & x > N_1 \delta, \end{cases}$$

where $f(x) = \frac{a}{2\delta} (\frac{b}{a}x + C)$, $C = 0.172$, and $h(x) = -\frac{ax}{\delta}$. The linear and scalar coefficients in (3.1) arise because we use a Fourier series to approximate the well function expression given in (2.2). In what follows we set $b = ka$ and then vary k to control the relative amplitude of well corrugation, as depicted by the diagram in Figure 2.3(A).

3.1. Numerical solutions for the mean first passage time and load-velocity relationship. As is customary for molecular motors, we are interested in calculating the force-velocity relation. In general, the velocity of the Kt motor with respect to an outside frame of reference must account for the internal velocity of the inserted kMT relative to the coupler. However, if the polymer-coupler assembly has reached an internal equilibrium or steady state (i.e., there is no motion of the tip relative to the binding sites), the velocity calculation is greatly simplified. This is because at steady state the ensemble of binding sites plus the polymer is moving with respect to an outside frame of reference at a velocity that is equal to the balance of kMT polymerization/depolymerization rates.

Before we start seeking steady state solutions we must recognize an important fact: with our current boundary conditions a steady state solution of (2.1) does not

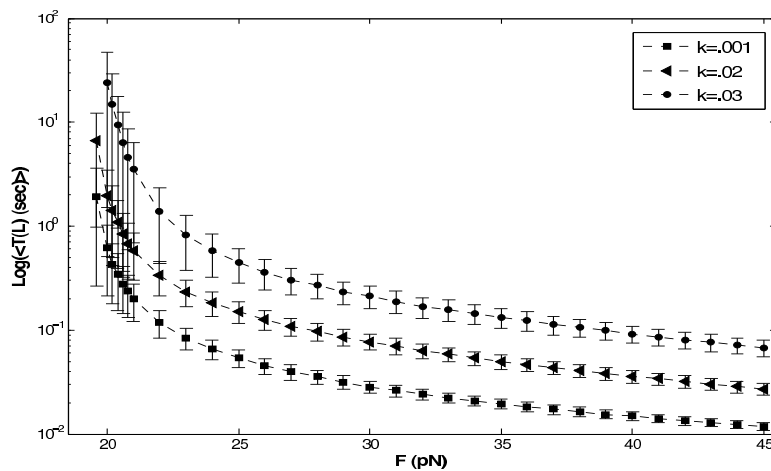


FIG. 3.1. Monte Carlo simulation results for the mean first exit times from $x = 0$, starting from $x = L$. Each curve represents the mean first exit time estimates for a given value of k , with $\beta_2 = 100 \text{ s}^{-1}$. Polymer tips start at $x = L$ at $t = 0$, and then the measured times for exit from the left boundary are averaged over 1000 trials for each F . The error bars mark the standard deviation. The maximum time allotted for exit was $T_{max} = 800 \text{ s}$. For $F < 19 \text{ pN}$ exit times exceeded T_{max} so computations were restricted to $F \geq 19 \text{ pN}$.

exist. This is because of the absorbing boundary condition at $x = 0$, which causes the polymer to eventually decouple. Nevertheless, if the polymer reaches a metastable position inside the coupler sufficiently far away from the absorbing boundary, we can safely approximate the $x = 0$ position as a reflecting barrier and solve for a steady state solution of (2.1). One way to determine the validity of this approximation is to determine the time it takes a polymer to find the absorbing boundary if it starts from some position in $(0, L)$. Thus, as a first step we formulate and then solve the mean first exit time problem for the polymer tip of an attached MT.

We let $T(x)$ be the mean time for exit through $x = 0$, starting from $x \leq L$. Then [3],

$$(3.2) \quad -1 = \frac{1}{\nu} V'(x) \partial_x T(x) + D \partial_x^2 T(x) + \alpha(x)(T(x+\delta) - T(x)) + \beta(x)(T(x-\delta) - T(x))$$

with boundary conditions $T(0) = 0$, $T'(L) = 0$.

The delay differential equation in (3.2) cannot be solved analytically; however, we can obtain an estimate for the solutions numerically. For our numerical studies we simulate a large number of Monte Carlo trials (1000 trials) of the Langevin equation in (2.1) for various model parameter values. For each trial we record the exit time, and then the results are averaged over the total number of paths tried.

In Figure 3.1 we show a plot of the Monte Carlo trials for the mean first exit times of the system for various loads F and activation energy levels, measured by the parameter k .

From Figure 3.1 we see that increases in motor loads significantly decrease the time for exit from the coupler. This is expected since forces $F > 0$ decrease x by counteracting the well's attractive forces, thus making it easier for the motor to escape through the absorbing boundary. From our simulations, we observe that for a wide range of loads the polymer does not exit the coupler for long times as compared to the relaxation time, i.e., $\langle T(L) \rangle > 100 \text{ s}$, whereas the time to relaxation to a steady

state is ≈ 1 s. Indeed, in Figure 3.1 simulations are shown only for $F \geq 19$ pN due to the large values of the first passage times that result when F is smaller than 19 pN. Thereby, a steady state approximation is appropriate for forces with large exit times. Further, when the activation energies increase, the system takes longer to escape from the absorbing boundary, as shown by the upward shifts in the mean first exit time curves in Figure 3.1 as k increases. These shifts can be explained by observing that for higher k it takes more energy for the polymer to detach from the coupler and hence more force is necessary to pull the polymer out of the chamber. For low activation energies ($k = 0.001$), the system is more “slippery” with metastable states occurring for a smaller range of loads with $F \leq 18$ pN. Our range of forces supported by the motors is in agreement with the predictions of [6]. Measurements of anaphase forces in meiotic grasshopper spermatocytes have produced maximal chromosomal forces on the order of 700 pN [12]. With our force estimates, we predict that for the total number of motors engaged in these chromosomes, we have 35×18 pN = 630 pN, which is consistent with experimental observations. Hence, we conclude that it is necessary to restrict the range of loads ($F \leq F_{\text{break}} \approx 18$ pN) for which the system can be examined at steady state and that the activation energies for the binding sites can significantly affect the range of forces that the motor can support.

Now that we have a range of loads for which the system equilibrates, we seek to find the kMT tip positions at steady state for various amounts of motor loads and Kt-MT binding strengths. The steady state positions can be obtained by solving the delay differential equation

$$(3.3) \quad 0 = -\frac{1}{\nu} \frac{\partial}{\partial x} (V'(x)p(x, t)) + D \frac{\partial^2}{\partial x^2} p(x, t) + \alpha(x - \delta)p(x - \delta, t) \\ + \beta(x + \delta)p(x + \delta, t) - (\alpha(x) + \beta(x))p(x, t).$$

Equation (3.3) cannot be solved analytically, but numerical solutions of the steady state distributions can be easily obtained with Monte Carlo simulations of the Langevin equation in (2.1). For each trial, we allow the system to relax into steady state and then record the final position of the kMT tip after some prescribed amount of time.

In Figures 3.2 and 3.3 we have plotted normalized histograms of the system at steady state for varying values of the parameter k and force F . In Figure 3.2 the plots are generated for a depolymerizing motor ($\beta_2 > \alpha_0$), whereas in Figure 3.3 the plots are generated for a polymerizing motor ($\beta_2 < \alpha_0$). In both rate regimes, as the activation energy increases, the polymer settles on average closer to $x = x_0$, the position where the kMT tip rates equilibrate with one another so that $\alpha(x_0) = \beta(x_0)$ ($x_0 \approx \beta_1$ for a depolymerizing motor, and $x_0 \approx \alpha_1$ for a polymerizing motor). For the highest barrier tried with $k = 0.08$, one immediately notices that the distributions are centered exactly at x_0 . This can be explained by noting that, for high activation barriers, the only way the system can transition down the potential well landscape is by jumping via the net Poisson jump rates given that the diffusion rate is too small to overcome the well barriers. Also, since the Poisson jumps control the equilibrium positions when k is large, it follows that the motor steady state positions are insensitive to motor loads, which when varied only alter the tilt and thus the minimum of the potential well function. On the other hand, if the well barriers are low, then diffusion is sufficient to transition the polymer tip to the minimum energy state of $\Psi(x)$ independent of the polymerization/depolymerization rates (as long as α, β are small). Further, in the low k limit, the positions where the distributions center in the well depend on the amount of load on the motor. As the pulling loads ($F > 0$) on the

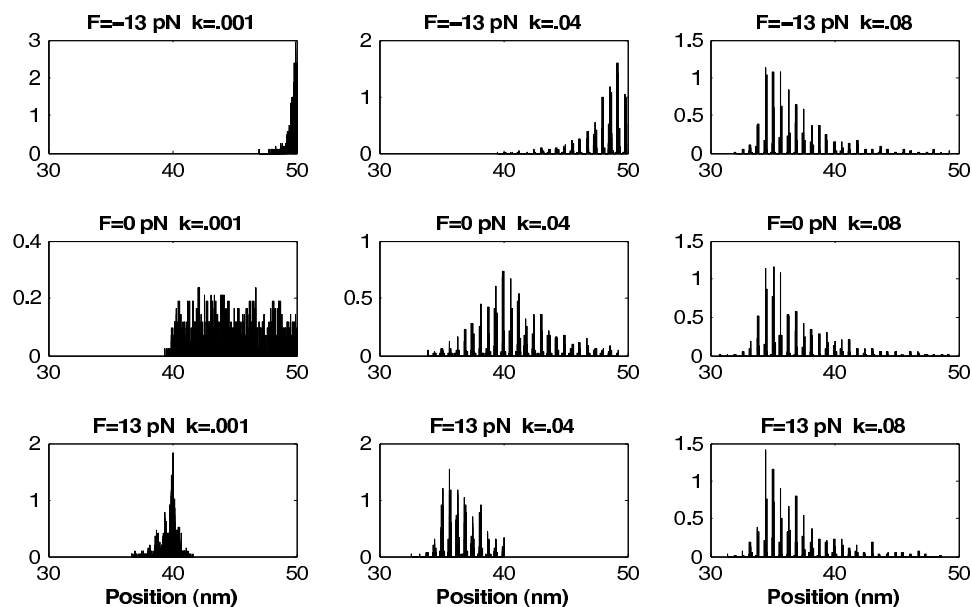


FIG. 3.2. Normalized histograms of the numerical simulation results with varying activation barriers and motor loads for a depolymerizing motor with $\beta_2 = 100 \text{ s}^{-1} > \alpha_0 = 80 \text{ s}^{-1}$. The histograms are generated by gathering simulation statistics for 1000 trials after relaxation into steady state.

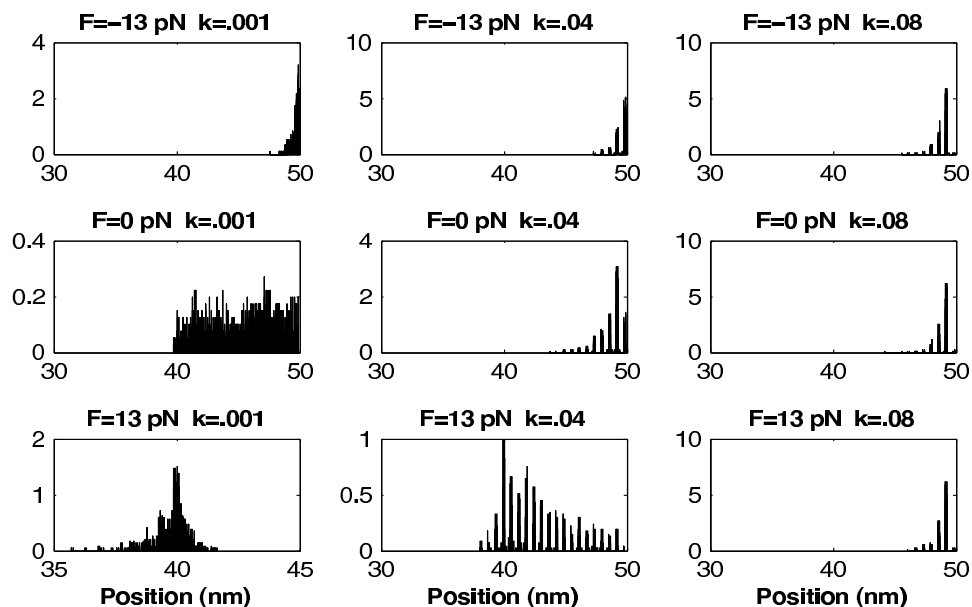


FIG. 3.3. Normalized histograms of the numerical simulation results with varying activation barriers and motor loads for a polymerizing motor $\beta_2 = 27 \text{ s}^{-1} < \alpha_0 = 80 \text{ s}^{-1}$. Each histogram is generated by gathering simulation statistics for 1000 trials after relaxation into steady state.

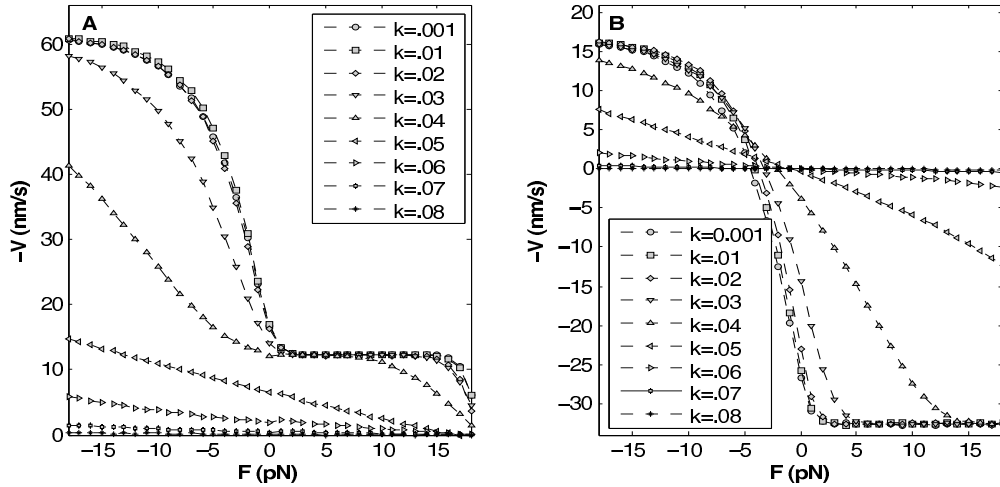


FIG. 3.4. Numerical load-velocity relationships for varying k . Velocities are obtained by averaging the numerical trial velocities, which are calculated by sampling the forward and backward jumps of the MT tip after the system relaxes into steady state. (A) Force-velocity calculations for a depolymerizing motor with $\beta_2 = 100 \text{ s}^{-1} > \alpha_0 = 80 \text{ s}^{-1}$. (B) Force-velocity calculations for a polymerizing motor with $\beta_2 = 27 \text{ s}^{-1} < \alpha_0 = 80 \text{ s}^{-1}$.

motor increase, the well loses its tilt and the peaks of the distributions relocate closer to $x = 0$. Whereas as the pushing loads increase ($F < 0$) in magnitude, the overlap bias is increased and the steady state distributions are pushed closer to the $x = L$ boundary (see the $k = 0.001$ panels in Figures 3.2 and 3.3). For intermediate $k = 0.04$, we see that the distributions are sensitive to the loads while also settling closer to x_0 . In summary, we deduce that the position of the peaks of the steady state probability distributions of kMT tips depend on the height of the unit activation barrier, k . If k is sufficiently small, then the distributions also depend on the motor loads, F .

We are now ready to calculate motor velocities. As noted at the beginning of this section, at steady state, the velocity of the system with respect to an outside frame of reference (let this frame have horizontal displacement measured by y) depends entirely on the net balance between the polymerization and depolymerization rates,

$$(3.4) \quad v = \delta \int (\alpha(y) - \beta(y)) p_s(y) dy,$$

with $p_s(y)$ the steady state distribution probability density for the position of the kMT tip. Equation (3.4) tells us that the motor velocity can be easily obtained by calculating the balance of the jump rates at the kMT tip steady state position. Therefore, even though we do not currently have analytic expressions for $p_s(y)$, we can obtain velocity values for a given load F from Monte Carlo simulations by sampling the forward and backward jump rates after the system reaches an equilibrium.

In Figure 3.4 we show load-velocity calculations from the simulations for various values of k .

From the load-velocity curves plotted in Figure 3.4 we see that the system produces distinct regions of constant velocity for a wide range of pulling loads when k is small ($k \leq 0.03$) for both polymerizing and depolymerizing motors. This can be explained by examining the steady state distributions in Figures 3.2 and 3.3. For low activation barriers, as the forces on the motor vary, the steady state distributions expe-

rience shifts on the x -axis. However, since at steady state the velocity depends only on the kMT polymerization/depolymerization rates, if the difference between $\alpha(x)$ and $\beta(x)$ is the same in the new shifted equilibrium position, then the motor velocity does not change. Consequently, there are flat velocity regions in the force-velocity curves for small k and $F > 0$ that keep the distributions in areas of constant net kMT rates. On the other hand, if we increase k , the flat regions in the force-velocity curves start to disappear. This happens because as k increases, the steady state distributions tend to center closer to the Poisson rate transition points β_1, α_1 . Being already located in sensitive regions, small perturbations in load can easily push the tip distributions on either side of the rate transition points and thus considerably disrupt the $\alpha(x), \beta(x)$ contribution to the velocity. Thus, the motors are more sensitive to loads, and the force-velocity relations become more uniformly monotone as k is increased as shown in Figure 3.4. Indeed, if we increase k enough, the steady state distributions become immobilized and center at exactly the rate transition points so that motor velocities decay to almost zero, resulting in the motor being stalled independent of load (see the force-velocity curves for $k = 0.08$).

The nonlinear force-velocity relations for $k \leq 0.03$ shown in Figure 3.4 are quite different from the typical linear force-velocity relations obtained for conventional motors such as kinesin and dynein. As noted above, the constant-velocity regions depend directly on the balance of kMT rates for a Kt motor. It follows that if we change the concentration of the kinase inside the motor by lowering β_2 , for example, then the force-velocity relation for the motor will shift down the velocity axis to reflect the change in the rate balance (compare the force-velocity curves for $k \leq 0.03$ in Figures 3.4(A) and 3.4(B)). Thus, variations in kMT depolymerization rates in the low k regime produce shifts in the force-velocity relations. This shift is significant when $\beta_2 < \alpha_0$ since motor velocities reverse signs, signaling a change in motor direction. This means that our motor model displays chemically controlled bidirectionality induced by modification of the depolymerase concentrations at the Kt. This feature of chemical control can be very useful when modeling chromosome movement during mitosis where both chemical and mechanical signals can create feedback for Kt motion control [15].

Next, we consider the monotone regions of the force-velocity relations for k small. By our convention for F values, if $F < 0$, the motor operates in the thermal ratchet regime. Under a large pushing load, the gap between the polymer tip and the Kt plate becomes very small, with steady state distributions equilibrating less than δ away from $x = L$. In this scenario, since there is little space between the polymer and the barrier, polymerization against the Kt plate is insignificant and motor velocities limit to $\delta\beta_2$. If β_2 is large, then motors experience rapid increments in depolymerizing velocity as F becomes more negative; see Figure 3.4(A). In the polymerizing motor case shown in panel (B) of Figure 3.4, this ratcheting effect is particularly prominent since it indicates that a polymerizing motor eventually transitions into a depolymerizing state (i.e., reverses direction of motion) when subjected to large negative pushing loads. On the other hand, if too much pulling load is placed on the motor (F large and positive), the polymer is pulled out of the chamber and velocities quickly decay due to steady state distribution shifts in regions where $\alpha_0 > \beta_0$ (note that for the polymerizing motor shown in Figure 3.4(B) for large $F > 0$, velocities remain constant because of our choice of $\beta_2 = \beta_0$).

In summary, our numerical solutions show that the jump-diffusion model proposed here produces constant motor velocities that are sensitive to kMT tip rate vari-

ations for weak binding (k small “slippery” regime), in agreement with experimental observations. We also found that when the activation barriers for detachment are increased, the motor transitions into stationary states where attachment is maintained against large loads as shown by the mean first exit time calculations. It is possible that this stalled or “sticky” motor regime is employed in cells where Kts need to maintain attachment under a significant increase in forces opposing movement. Our model shows that attachment robustness can be greatly improved by increasing binding affinities of the Kt binders; however, the robustness is achieved at the expense of velocity. Experimental work has shown that the inhibition of phosphorylation of Ndc80 binding filaments by Aurora B kinases at Kts increases the binding affinity of the linkers to the kMT lattice and also results in Kts being immobilized on the kMT lattice [2]. Our model predicts that this observed immobility could be the result of only changes in filament affinity for the kMT lattice, independent of the polymerization/depolymerization dynamics of the inserted polymer tip. In the second part of this paper we will see that variations in the spatial distribution of Kt binders on the MT lattice can dramatically change motor response to changes in the parameter k .

4. Asymptotic approximation. From the simulations of the jump-diffusion model, we see that the height of the activation energy barrier between binding sites can greatly affect motor motion characteristics. However, Monte Carlo simulations are computationally expensive so it would be useful to explore parameter ranges for which analytical expressions for the force-velocity relationship can be derived. In this section we use homogenization theory in order to obtain simpler approximate analytical force-velocity relation expressions for the Kt motor model.

Since we are ultimately interested in determining the force-velocity relation for the motor, the equation of interest for approximation is the steady state equation for the probability density which reads

$$(4.1) \quad 0 = -\frac{1}{\nu} \frac{\partial}{\partial x} \left[\left(f(x) \cos \left(\frac{2\pi x}{\delta} \right) + r(x) \right)' p(x) \right] + Dp_{xx}(x) - (\alpha(x) + \beta(x))p(x) + \beta(x + \delta)p(x + \delta) + \alpha(x - \delta)p(x - \delta),$$

where we have used the expression in (3.1) for $\Psi(x)$ and $r(x) = -f(x) - h(x) - Fx$.

We start by Taylor expanding the jump terms, which introduces an infinite sum term in (4.1). Then, using the no flux boundary conditions, we integrate (4.1) once to obtain

$$(4.2) \quad 0 = -\frac{1}{\nu} \left(f(x) \cos \left(\frac{2\pi x}{\delta} \right) + r(x) \right)' p(x) + Dp_x(x) + \sum_{n=1}^{\infty} \frac{\delta^n}{n!} \frac{d^{n-1}}{dx^{n-1}} \left((\beta(x) + (-1)^n \alpha(x)) p(x) \right).$$

From the numerical solutions of the steady state distributions, we notice that the solution to (4.2) should contain high frequency periodic oscillations with a slow varying amplitude. In order to identify equation terms which evolve on different spatial scales, it is necessary to rescale space in (4.2). We set $x = Xy = \frac{\nu D \delta}{b} y$, where y is a

dimensionless variable. In terms of the variable y the steady state equation reads

$$(4.3) \quad 0 = - \left(\hat{f}(y) \cos \left(\frac{2\pi y}{\varepsilon} \right) + \hat{r}(y) \right)' p(y) + p_y(y) + \alpha_2 \sum_{n=1}^{\infty} \frac{\varepsilon^{n-1}}{n!} \frac{d^{n-1}}{dy^{n-1}} \left(\left(\hat{\beta}(y) + (-1)^n \hat{\alpha}(y) \right) p(y) \right),$$

where we identify $\varepsilon = \frac{b}{k_B T}$ as the small dimensionless parameter and $\alpha_2 = \frac{\beta_0 \delta^2 \nu}{b}$. Also, $\hat{f}(y) = f(y)/\nu D$, $\hat{r}(y) = r(y)/\nu D$, $\hat{\beta}(y) = \beta(y)/\beta_0$, $\hat{\alpha}(y) = \alpha(y)/\beta_0$. Note that this change of variables allowed us to rewrite the oscillatory part of the drift term as a high frequency periodic oscillator with a slow varying amplitude.

Following the multiscale technique, we now introduce two spatial variables: a “slow” variable $z = y$ and a “fast” variable $\sigma = \frac{y}{\varepsilon}$. Immediately, we see that the drift term in (4.3) contains fast oscillations with a slow varying amplitude.

Next, we treat z and σ as independent variables and by the chain rule, $\frac{d}{dy} = \frac{\partial}{\partial z} + \frac{1}{\varepsilon} \frac{\partial}{\partial \sigma}$. The equation now becomes

$$(4.4) \quad 0 = - \left(\hat{f}'(z) \cos(2\pi\sigma) + \hat{r}'(z) - \frac{2\pi}{\varepsilon} \hat{f}(z) \sin(2\pi\sigma) \right) p(z) + p_z(z) + \frac{1}{\varepsilon} p_\sigma(z) + \alpha_2 \sum_{n=1}^{\infty} \frac{\hat{\beta}(z) + (-1)^n \hat{\alpha}(z)}{n!} \frac{\partial^{n-1}}{\partial \sigma^{n-1}} p(z, \sigma) + \varepsilon \alpha_2 \sum_{n=2}^{\infty} \frac{(n-1)}{n!} \frac{\partial}{\partial z} \frac{\partial^{n-2}}{\partial \sigma^{n-2}} \left(\left(\hat{\beta}(z) + (-1)^n \hat{\alpha}(z) \right) p(z) \right) + O(\varepsilon^2).$$

As is customary for the multiscale method, we seek a solution that can be written as an asymptotic series $p(z) = p_0(z, \sigma) + \varepsilon p_1(z, \sigma) + O(\varepsilon^2)$, where $p_0(z, \sigma)$ represents the mean field and p_1 has zero mean value in z and is periodic in σ , with period 1. Substituting the expansion for $p(z)$ into (4.4) and collecting same order terms we obtain the following hierarchy of equations:

$$(4.5) \quad O\left(\frac{1}{\varepsilon}\right) : 2\pi \hat{f}(z) \sin(2\pi\sigma) p_0(z, \sigma) + p_{0\sigma}(z, \sigma) = 0,$$

$$(4.6) \quad O(1) : 2\pi \hat{f}(z) \sin(2\pi\sigma) p_1(z, \sigma) + p_{1\sigma}(z, \sigma) - \left(\hat{f}'(z) \cos(2\pi\sigma) + \hat{r}'(z) \right) p_0(z, \sigma) + p_{0z}(z, \sigma) + \alpha_2 \sum_{n=1}^{\infty} \frac{1}{n!} \left(\hat{\beta}(z) + (-1)^n \hat{\alpha}(z) \right) \frac{\partial^{n-1}}{\partial \sigma^{n-1}} p_0(z, \sigma) = 0.$$

Finally, the probability densities need to be normalized, with

$$(4.7) \quad 1 = \int_0^{L/X} \left(p_0(z, \sigma) + \varepsilon p_1(z, \sigma) \right) dz.$$

We solve (4.5) by direct integration to obtain

$$(4.8) \quad p_0(z, \sigma) = A_0(z) \exp \left(\hat{f}(z) \cos(2\pi\sigma) \right).$$

Next, we examine the infinite sum term in (4.6). For a fixed arbitrary value of $z = z_0$, we define $F(\sigma) = \int_0^\sigma p_0(z_0, \eta) d\eta$. Taylor expansion of $F(\sigma)$ gives

$$(4.9) \quad \int_0^1 p_0(z_0, \eta) d\eta = F(\sigma + 1) - F(\sigma) = \sum_{n=1}^\infty \frac{1}{n!} \frac{\partial^n}{\partial \sigma^n} \left(\int_0^\sigma p_0(z_0, \eta) d\eta \right),$$

$$(4.10) \quad - \int_0^1 p_0(z_0, \eta) d\eta = F(\sigma - 1) - F(\sigma) = \sum_{n=1}^\infty \frac{(-1)^n}{n!} \frac{\partial^n}{\partial \sigma^n} \left(\int_0^\sigma p_0(z_0, \eta) d\eta \right),$$

where we have used the periodicity of $p_0(z, \sigma)$ in σ for a fixed $z = z_0$.

Substituting the expressions from (4.9)–(4.10) into the $O(1)$ equation, we have

$$(4.11) \quad O(1) : 2\pi \hat{f}(z) \sin(2\pi\sigma) p_1(z, \sigma) + p_{1\sigma}(z, \sigma) - \left(\hat{f}'(z) \cos(2\pi\sigma) + \hat{r}'(z) \right) p_0(z, \sigma) + p_{0z}(z, \sigma) + \alpha_2 \left(\hat{\beta}(z) - \hat{\alpha}(z) \right) \int_0^1 p_0(z, \sigma) d\sigma = 0.$$

We solve for the coefficient $A_0(z)$ by examining the $O(1)$ equation (4.11). Since we are looking for a solution $p_1(z, \sigma)$ that is periodic in σ , we impose the following solvability condition on (4.11):

$$(4.12) \quad 0 = \int_0^1 \left((p_1(z, \sigma) I(z, \sigma))_\sigma + \exp(\hat{r}(z)) \left(p_0(z, \sigma) \exp(-\hat{r}(z)) I(z, \sigma) \right)_z + \alpha_2 \left(\hat{\beta}(z) - \hat{\alpha}(z) \right) \int_0^1 p_0(z, \eta) d\eta I(z, \sigma) \right) d\sigma = -\hat{r}'(z) A_0(z) + A_0'(z) + \alpha_2 A_0(z) \left(\hat{\beta}(z) - \hat{\alpha}(z) \right) I_0^2(\hat{f}(z)),$$

where $I(z, \sigma) = \exp(-\hat{f}(z) \cos(2\pi\sigma))$ and $I_0(\hat{f}(z))$ is the integral form of the modified Bessel function of the first kind.

Therefore,

$$(4.13) \quad A_0(z) = \hat{C} \exp \left(\hat{r}(z) - \alpha_2 \int I_0^2(\hat{f}(z)) \left(\hat{\beta}(z) - \hat{\alpha}(z) \right) dz \right).$$

Finally, in terms of our original variable x , this yields the solution

$$(4.14) \quad p_0(x) = C \exp \left(\frac{V(x)}{k_B T} - \frac{\delta\nu}{k_B T} \int I_0^2 \left(\frac{f(x)}{k_B T} \right) \left(\beta(x) - \alpha(x) \right) dx \right),$$

where the coefficient C is found from the normalization condition for the probability densities in (4.7).

Therefore, our approximation for the probability density function at steady state is

$$(4.15) \quad p(x) \approx C \exp \left(\frac{V(x)}{k_B T} - \frac{\delta\nu}{k_B T} \int I_0^2 \left(\frac{f(x)}{k_B T} \right) \left(\beta(x) - \alpha(x) \right) dx \right) + O(\varepsilon).$$

With the steady state solutions for the system in (4.15), we can readily calculate

motor velocities using

(4.16)

$$\begin{aligned} v &\approx v_0 + O(\varepsilon) \\ &= \delta \int_0^L (\alpha(x) - \beta(x)) p_0(x) dx + O(\varepsilon) \\ &= \delta C \int_0^L (\alpha(x) - \beta(x)) \exp\left(\frac{V(x)}{k_B T} - \frac{\delta \nu}{k_B T} \int I_0^2\left(\frac{f(x)}{k_B T}\right) (\beta(x) - \alpha(x)) dx\right) dx \\ &\quad + O(\varepsilon). \end{aligned}$$

The integral expression for the approximation of motor velocities given in (4.16) contains a fast oscillating term in the integrand, which creates difficulties in numerical calculations. We can further simplify the velocity expression by deriving an approximation for $v_0(x)$ using a modification of the method of averaging [8].

To find the velocity, we want to solve the initial value problem

$$(4.17) \quad \frac{dV(x)}{dx} = \delta(\alpha(x) - \beta(x)) p_0(x),$$

$$(4.18) \quad V(0) = 0,$$

where we are interested in evaluating $V(L)$.

Using the same rescaling for space with $x = Xy$, we again introduce the fast and slow variables $y = z$, $\sigma = \frac{y}{\varepsilon}$. With this change of variables the problem reads

$$(4.19) \quad \frac{dV(z, \sigma)}{dz} = \delta(\alpha(z) - \beta(z)) p_0(z, \sigma),$$

$$(4.20) \quad V(0) = 0.$$

We now assume a solution of the form $V(z, \sigma) = V_0(z) + \varepsilon V_1(z, \sigma)$ with $V_1(z, \sigma)$ periodic in σ . Notice that $V_0(z)$ represents the mean field so that $V_1(z, \sigma)$ has zero mean in z . Substituting the expansion into (4.19) and retaining the $O(1)$ terms yields

$$(4.21) \quad \frac{dV_0(z)}{dz} + \frac{dV_1(z, \sigma)}{d\sigma} = \delta(\alpha(z) - \beta(z)) p_0(z, \sigma).$$

Recalling that V_1 is periodic in σ , it follows that

$$(4.22) \quad \int_0^\sigma \left(\frac{\partial V_0(z)}{\partial z} + \frac{\partial V_1(z, \eta)}{\partial \eta} \right) d\eta = \frac{\partial V_0}{\partial z} \sigma,$$

which in turn produces

$$(4.23) \quad \frac{\partial V_0(z)}{\partial z} = \frac{1}{\sigma} \int_0^\sigma \delta(\alpha(z) - \beta(z)) p_0(z, \eta) d\eta = \delta(\alpha(z) - \beta(z)) \overline{p_0(z, \sigma)}.$$

Substituting $\sigma = 1$, we obtain the first order approximation to the solution

$$(4.24) \quad \begin{aligned} \frac{dV_0(z)}{dz} &= \delta(\alpha(z) - \beta(z)) \exp\left(\hat{r}(z) - \alpha_2 \int I_0^2(\hat{f}(z)) (\hat{\beta}(z) - \hat{\alpha}(z)) dz\right) \\ &\quad \times \int_0^1 \exp(\hat{f}(z) \cos(2\pi\sigma)) d\sigma. \end{aligned}$$

We immediately recognize that the integral expression in (4.24) is the integral form of the modified Bessel function of the first kind, $I_0(\hat{f}(z))$; therefore we can now write an explicit solution for the velocity of the coupler,

$$\begin{aligned}
 (4.25) \quad v &= V(L) \\
 &= \delta \int_0^L (\alpha(x) - \beta(x)) \exp\left(\frac{r(x)}{k_B T} - \frac{\delta\nu}{k_B T} \int I_0^2\left(\frac{f(x)}{k_B T}\right) (\beta(x) - \alpha(x)) dx\right) \\
 &\quad \times I_0\left(\frac{f(x)}{k_B T}\right) dx + O(\varepsilon).
 \end{aligned}$$

Next, we observe that the approximate solution, $p_0(x)$, is the steady state solution of the Fokker–Planck equation,

$$\begin{aligned}
 (4.26) \quad \frac{\partial p_0(x, t)}{\partial t} &= -\frac{1}{\nu} \frac{\partial}{\partial x} \left[\left(V'(x) - \delta\nu I_0^2\left(\frac{f(x)}{k_B T}\right) (\beta(x) - \alpha(x)) \right) p_0(x, t) \right] \\
 &\quad + D \frac{\partial^2}{\partial x^2} p_0(x, t),
 \end{aligned}$$

with appropriate boundary conditions. Thereby, by setting out to derive an asymptotic approximation, we have also gained a reduction of the jump-diffusion motor model into a simpler drift-diffusive model. The advantage of this approach is that for the approximate drift-diffusive process not only can we calculate the velocity explicitly, but also the mean first passage time problem is greatly simplified and can be obtained analytically. In what follows, we derive analytical solutions for the mean first exit time calculation starting with the approximate drift-diffusion model.

From the Fokker–Planck equation given in (4.26), we obtain the following ordinary differential equation for the first passage time $T(x)$ at $x = 0$:

$$(4.27) \quad \frac{1}{\nu} \left(V'(x) - \delta\nu I_0^2\left(\frac{f(x)}{k_B T}\right) (\beta(x) - \alpha(x)) \right) \partial_x T(x) + D \partial_x^2 T(x) = -1$$

with boundary conditions $T(0) = 0$, $T'(L) = 0$ as before. Note that since the delay terms do not appear in this case we can use direct integration to obtain the solution for the mean first exit time

$$\begin{aligned}
 (4.28) \quad T(x) &= \frac{1}{D} \int_0^x \exp\left(-\frac{V(y)}{k_B T} + \frac{\delta\nu}{k_B T} \int I_0^2\left(\frac{f(y')}{k_B T}\right) (\beta(y') - \alpha(y')) dy'\right) \\
 &\quad \times \int_y^L \exp\left(\frac{V(z)}{k_B T} - \frac{\delta\nu}{k_B T} \int I_0^2\left(\frac{f(z')}{k_B T}\right) (\beta(z') - \alpha(z')) dz'\right) dz dy.
 \end{aligned}$$

The underlying assumption for our asymptotic approximation so far has been that ε is sufficiently small in order for our approximate solutions to be accurate. Recall that $\varepsilon = \frac{b}{k_B T}$, which means that b has to be small and, since $b = ka$, the parameter k must be small. This conclusion is in agreement with our intuition, since the jump-diffusion process we started with can be expected to reduce to a diffusive process we obtained in (4.26) only if the unit activation barrier in the $\Psi(x)$ term is sufficiently small, so that the diffusive steps can overcome the Poisson noise. As we show below, $k = 10^{-3}$ is sufficiently small for our diffusive approximation to exactly match the numerics of the full jump-diffusion model.

In Figure 4.1 we have plotted a comparison between the approximate steady state solutions $p_0(x)$ and the histograms we obtained numerically in the previous section

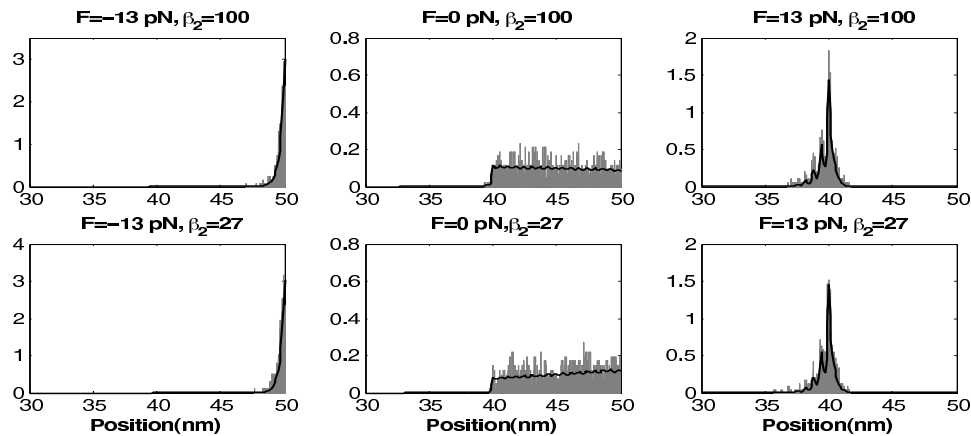


FIG. 4.1. A comparison of the numerical versus the analytical steady state distributions for the diffusive approximation of the steady state probability density function for varying loads F and $k = 0.001$.

for $k = 0.001$ for both a polymerizing and a depolymerizing motor. As can be seen from Figure 4.1, our analytical steady state solutions are in very good agreement with the numerical simulation of the full jump-diffusion model for small k .

Next, a comparison between the load-velocity relationships from (4.16) and the numerical calculations for the velocity presented in the previous section is given in Figure 4.2(A).

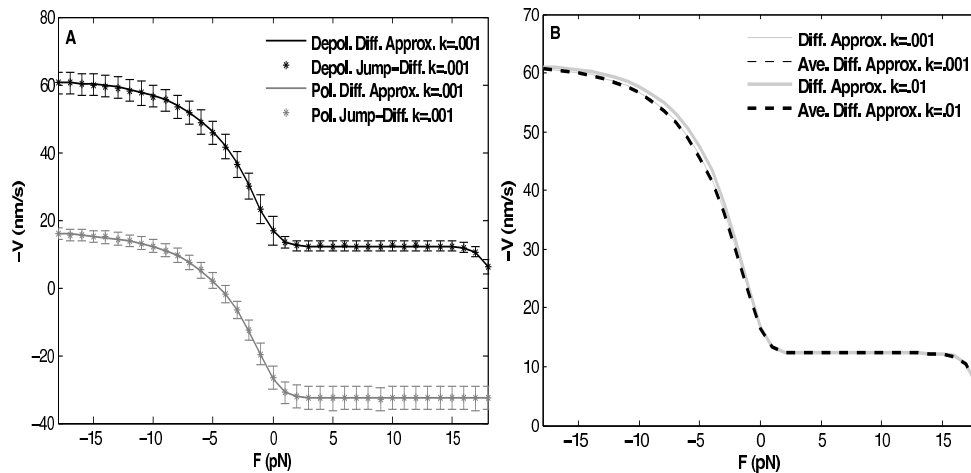


FIG. 4.2. (A) Load-velocity relationship comparison between the diffusive approximation $v_0(x)$ and the Monte Carlo simulations for $k = 0.001$ for a depolymerizing and a polymerizing motor. For the numerical simulations, bars represent the standard deviation. (B) Load-velocity relationship comparison between the diffusive approximation load-velocity relationship as given in (4.16) and the averaged velocity in (4.25) for $k = 0.001$ and $k = 0.01$.

From Figure 4.2(A) we see that for small barriers with $k = 0.001$, the analytic solution v_0 is in excellent agreement with the numerical results obtained for the full jump-diffusion model. This approximation remains in very good agreement for $k = 0.01$; however, the plot is not shown for clarity as these plots overlay one another. For

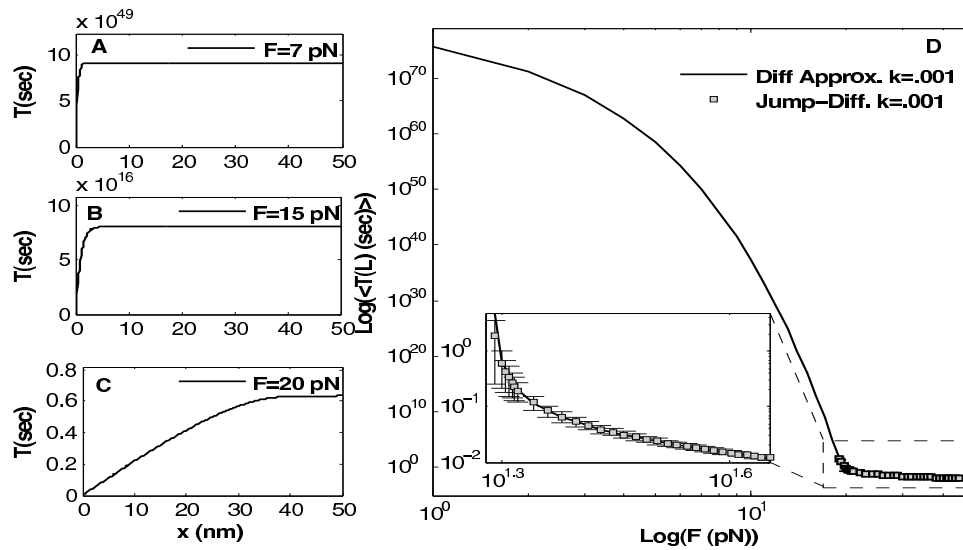


FIG. 4.3. Mean first exit time calculation for the approximate diffusive model for $k = 0.001$. (A) Mean time for exit, $T(x)$ from the boundary $x = 0$ starting from x , measured in sec for $F = 7$ pN. (B) Mean time for exit for $F = 15$ pN. (C) Mean time for exit for $F = 15$ pN. (D) Log-log plot of mean first passage time through $x = 0$ starting from $L = 50$ nm versus motor load F . Inset: Comparison of the analytical solutions with the numerical results.

$k > 0.01$, the diffusive limit solutions lose their accuracy and thus cannot be used to compare with the numerical calculations. Further, in panel (B) of Figure 4.2 we see that the averaged velocity expression in (4.25) is in very good agreement with (4.15) for $k = 0.001$ and is also a good approximation for $k = 0.01$.

In Figures 4.3(A)–4.3(C) we have plotted the mean first exit time solution in (4.28) for varying force terms F with respect to the initial position x . Notice from the plots that it takes a very long time for the tip to leave the coupler for small pulling forces, and thus we consider the system to have reached a metastable state in panels (A) and (B) of Figure 4.3. However, for larger pulling loads (panel (C)) the exit times decrease significantly indicating that the forces are approaching the breaking loads for the motor. Thus, the mean first exit time calculation in the diffusive limit gives us a way to analytically determine the system breaking loads.

In panel (D) of Figure 4.3 we show a log-log plot of first exit times through $x = 0$ starting from $x = L$, with respect to varying load F . From Figure 4.3(D) we observe that our numerical results from section 3.1 and the analytical solution for the exit times in (4.28) agree well with each other. Furthermore, panel (D) shows that our mean first exit time approximation experiences a sharp decline in exit times past $F = 18$ pN in agreement with our numerical results for breaking loads.

In conclusion, in this section we have shown that for small k , analytical expressions for the force-velocity relation can be obtained which are in good agreement with our numerical simulations. The parameter range for which we obtained analytical approximate solutions falls within the range of experimental predictions for Kt binding. Recent measurements of the diffusion coefficients of several MT binding proteins which are involved in Kt-MT binding seem to indicate that their activation energy for MT binding is indeed very low [17], and thus the diffusive limit we explore here might be a good approximate model for the interaction of the Kt coupler with a dynamic microtubule polymer.

5. The off-register well. So far, we have discussed the case when the spacing of Kt binders is an integer multiple of the binding site spacing on the MT lattice, δ . However, the exact geometry of the Kt binder elements on the attached MT lattice is not yet known. Therefore, alternate scenarios for the spacing between Kt linkers must be considered. If the Kt binders are not in-register with the binding sites on the polymer, then the Kt bound coupler linkers need not be all detached for a new attachment to be established. As a result, the geometry of the potential well is altered and two well parameters are important: s , the linker spacing which establishes the period of free energy drops due to binding events in the well, and δ , which establishes the period of transitions between the individual activation barriers. In the remainder of this paper we examine the case in which the linkers are spaced with distances that are not integer multiples of δ with $s = \bar{\kappa}\delta = \frac{1}{\bar{\kappa}}\delta = \frac{3\sqrt{2}}{2}\delta$: the off-register well case.

We use a Fourier series approximation for the off-register well $\Psi(x)$, which reads

$$(5.1) \quad \Psi(x) = \begin{cases} -aC_1 \sin\left(\frac{2\pi x}{s}\right) + bC_2 g(x) - bC_3 \cos\left(\frac{2\pi x}{s}\right) + h(x), & x \leq N_2 s, \\ -bC_3 + bC_2 g(x) + h(N_2 s), & x > N_2 s, \end{cases}$$

with $h(x) = -\frac{a}{2}C_{20}x$ and $g(x) = \cos\left(\frac{2\pi(x-(N_2+1/2)s)}{\delta}\right) - \cos\left(\frac{2\pi(x+s/2)}{\delta}\right)$. The coefficients from the approximation are as follows: $C_{20} = 1.5$, $C_1 = 0.17$, $C_2 = 2.7$, $C_3 = 0.01$.

5.1. Numerical calculation of the force-velocity relation. The steady state expression in (3.3) with the well function of (5.1) can be solved numerically using Monte Carlo simulations we described in section 3.1. The new well shape significantly affects how the motor responds to increases in individual activation barriers, b .

Numerical solutions for the steady state distributions with the off-register well are shown in Figures 5.1 and 5.2. For all the values of k that we consider in our study, the numerical solutions for the steady state distributions settle at the lowest energy state of the potential well for both a polymerizing and depolymerizing off-register motor as shown in Figures 5.1 and 5.2. Recall that the forces F change the well tilt and thus affect the position of the lowest energy state in the well; thereby we see shifts on the x -axis as the motor loads are varied. These steady state results are quite different from what we saw for the in-register well in the previous section where high k values affected the steady state histograms. This is due to the new well shape which does not hinder diffusion of the kMT tip to the lowest binding energy state since the increases in the individual barriers are not amplified significantly as the overlap increases.

Next, we numerically determine motor velocities for various motor loads at steady state. In Figure 5.3 we have plotted the force-velocity relation for the motor with the off-register well for different values of the parameter k . The plots are obtained using Monte Carlo simulations as in section 3.1. We observe that there are some differences in motor response when the well function is altered to be off-register. Namely, the force-velocity relations do not show a slow down in velocity as we increase the value of the parameter k . This is to be expected, since the new topology of the well changes how the steady state histograms respond to variations in the value of k , as we saw in Figures 5.1 and 5.2. For all the k we have tested here the steady state distribution histograms experience shifts on the x -axis and accordingly the force-velocity curves show flat regions corresponding to loads that cause shifts in regions where the net balance of rates is unchanged. As a result, both a polymerizing and a depolymerizing

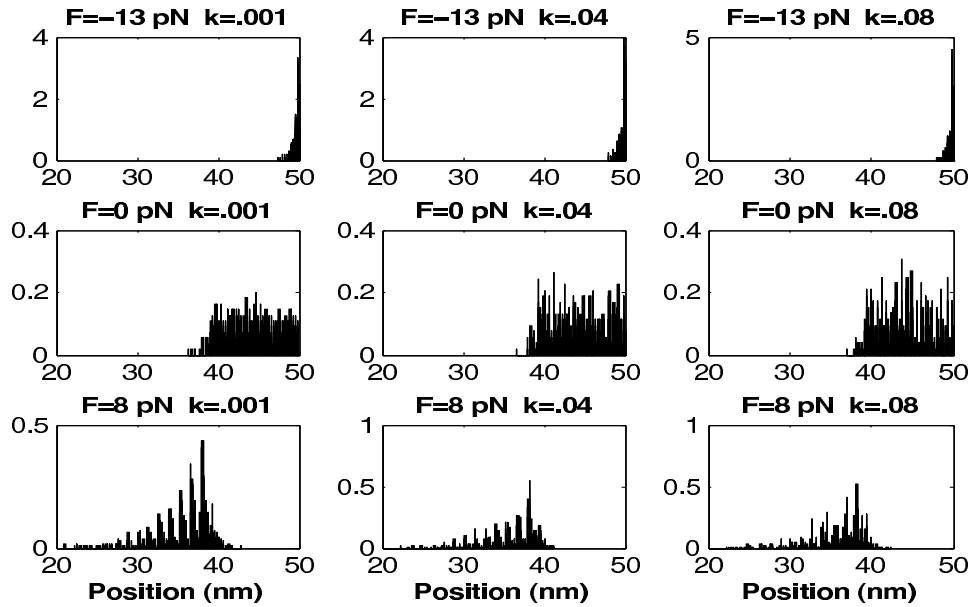


FIG. 5.1. Off-register well normalized histograms of the numerical simulation results with varying activation barriers and motor loads for a depolymerizing motor with $\beta_2 = 100 \text{ s}^{-1} > \alpha_0 = 80 \text{ s}^{-1}$. Each histogram is generated by gathering simulation statistics for 1000 trials after relaxation into steady state.

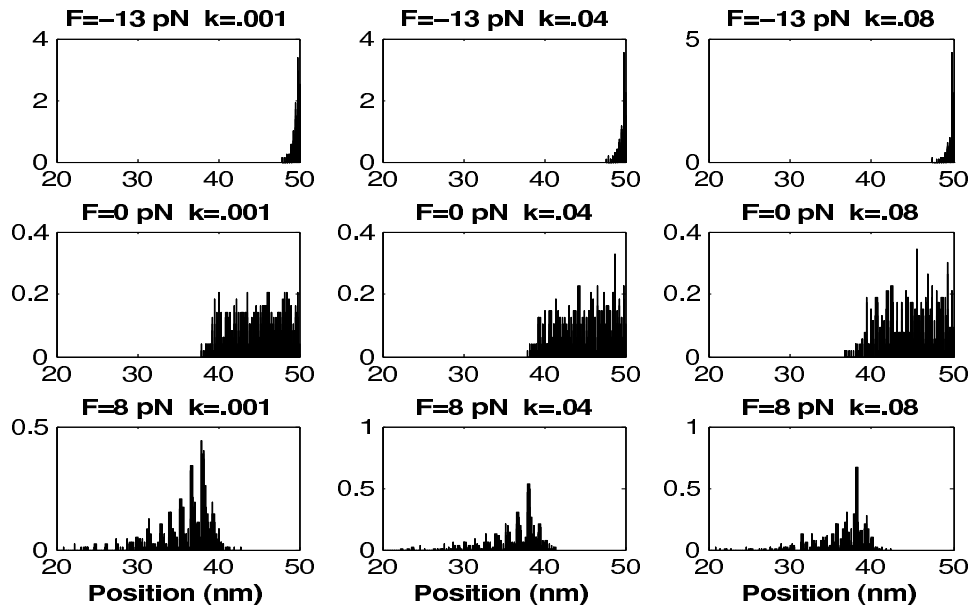


FIG. 5.2. Off-register well normalized histograms of the numerical simulation results with varying activation barriers and motor loads for a polymerizing motor with $\beta_2 = 27 \text{ s}^{-1} < \alpha_0 = 80 \text{ s}^{-1}$. Each histogram is generated by gathering simulation statistics for 1000 trials after relaxation into steady state.

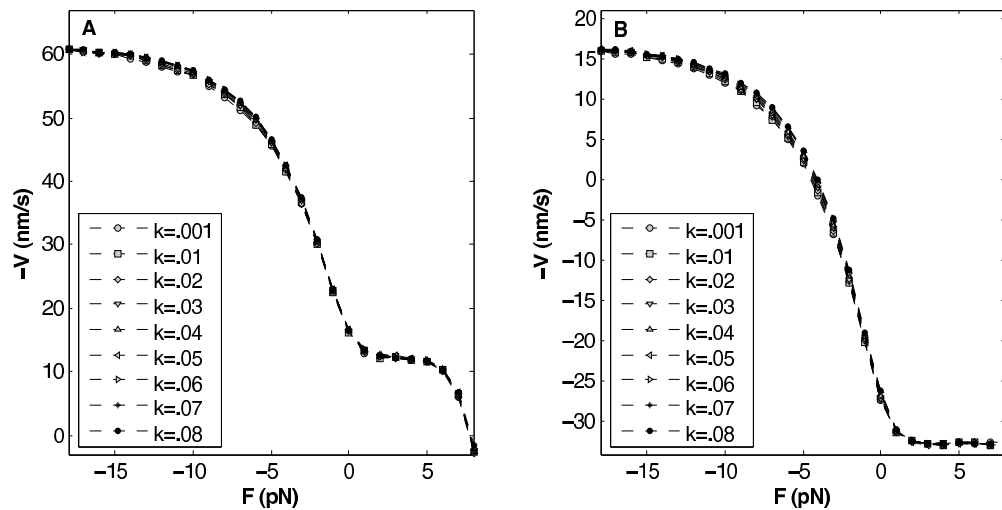


FIG. 5.3. Numerical load-velocity relationships for varying energy barriers for the off-register well. (A) Force-velocity calculations for a depolymerizing motor with $\beta_2 = 100 \text{ s}^{-1} > \alpha_0 = 80 \text{ s}^{-1}$. (B) Force-velocity calculations for a polymerizing motor with $\beta_2 = 27 \text{ s}^{-1} < \alpha_0 = 80 \text{ s}^{-1}$.

motor with an off-register well can display only a slippery or “floating grip” velocity mode.

Finally, the change of the well function also causes the breaking loads for the system to decrease. This is because with the given value of s we can fit only about half the number of binders on the MT lattice when the coupler is fully engaged (note that $F \leq 8 \text{ pN}$ in Figure 5.3). Since the motor breaking load needs to overcome the total energy of binding to detach a coupler, a reduction in the total number of binders results in a decrease in the amount of load required to detach the MT polymer from the Kt.

5.2. Asymptotic approximation. The simulations of the off-register case indicate that the motor remains in the slippery regime despite changes in the unit activation barrier values. Based on our previous calculations, we expect that in the off-register case the drift-diffusion approximation can be a good model approximation for a wider range of k values. Accordingly, in this section, we repeat the homogenization argument for the off-register well in order to derive analytic expressions for the force-velocity relation.

We repeat our steps from section 4 with the off-register well. After integrating once with the no-flux boundaries, the steady state equation with the new well function yields

$$(5.2) \quad 0 = -\frac{1}{\nu} \left(aC_1 \sin \left(\frac{2\pi x}{s} \right) - bC_2 g(x) + bC_3 \cos \left(\frac{2\pi x}{s} \right) + r(x) \right)' p(x) + Dp_x(x) \\ + \sum_{n=1}^{\infty} \frac{\delta^n}{n!} \frac{d^{n-1}}{dx^{n-1}} \left((\beta(x) + (-1)^n \alpha(x)) p(x) \right),$$

where $r(x) = -h(x) - Fx$.

As before, we rescale space by setting $x = Xy = \frac{\nu D \delta}{b} y$, and (5.2) reads

$$(5.3) \quad 0 = - \left(\frac{aC_1}{k_B T} \sin(2\pi\kappa\sigma) - \varepsilon C_2 g(2\pi\sigma) + \varepsilon C_3 \cos(2\pi\kappa\sigma) + \hat{r}(y) \right)' p(y) + p_y(y) + \alpha_2 \sum_{n=1}^{\infty} \frac{\varepsilon^{n-1}}{n!} \frac{d^{n-1}}{dy^{n-1}} \left((\hat{\beta}(y) + (-1)^n \hat{\alpha}(y)) p(y) \right).$$

This time, we assume the existence of a solution with the expansion $p(y) = p_0(y, \sigma) + \varepsilon p_1(y, \sigma) + O(\varepsilon^2)$, where we now require $p_1(y, \sigma)$ to be a bounded function. In accordance with our previous derivation we introduce two spatial variables: a “slow” variable $z = y$ and a “fast” variable $\sigma = \frac{y}{\varepsilon}$.

The hierarchy of equations after substituting the assumed asymptotic solution expansion into (5.3) is

$$(5.4) \quad O\left(\frac{1}{\varepsilon}\right) : - \left(\frac{2\pi a C_1}{k_B T} \cos(2\pi\kappa\sigma) \right) p_0(z, \sigma) + p_{0\sigma}(z, \sigma) = 0,$$

$$(5.5) \quad O(1) : - \left(\frac{2\pi a C_1}{k_B T} \cos(2\pi\kappa\sigma) \right) p_1(z, \sigma) + p_{1\sigma}(z, \sigma) - \left(\hat{r}'(z) - 2\pi C_3 \sin(2\pi\kappa\sigma) - C_2 g'(2\pi\sigma) \right) p_0(z, \sigma) + p_{0z}(z, \sigma) + \alpha_2 \left(\hat{\beta}(z) - \hat{\alpha}(z) \right) \int_0^1 p_0(z, \sigma) d\sigma = 0.$$

First, we see that the solution of the $O\left(\frac{1}{\varepsilon}\right)$ equation can be obtained, as before, by direct integration, where we get

$$(5.6) \quad p_0(z, \sigma) = A_0(z) \exp\left(\frac{aC_1 \sin(2\pi\kappa\sigma)}{k_B T}\right).$$

Note that $p_1(z, \sigma)$ is only required to be bounded, so after solving the $O(1/\varepsilon)$ equation, we have to check that the $O(1)$ equation indeed satisfies the required boundedness requirement. This last step allows us to obtain an expression for the coefficient $A_0(z)$. Let

$$(5.7) \quad I(z, \sigma) = \exp\left(-\frac{aC_1 \sin(2\pi\kappa\sigma)}{k_B T}\right),$$

and the $O(1)$ equation can now be written as

$$(5.8) \quad 0 = \left(p_1(z, \sigma) I(z, \sigma) \right)_\sigma + \exp(\hat{r}(z)) \left(p_0(z, \sigma) \exp(-\hat{r}(z)) I(z, \sigma) \right)_z + \left(C_2 g'(2\pi\sigma) + 2\pi C_3 \sin(2\pi\kappa\sigma) \right) A_0(z) + \alpha_2 \left(\hat{\beta}(z) - \hat{\alpha}(z) \right) A_0(z) I(z, \sigma) I_0\left(\frac{aC_1}{k_B T}\right),$$

where $I_0\left(\frac{aC_1}{k_B T}\right)$ again denotes the integral form of the modified Bessel function of the

first kind, this time evaluated at $\hat{f}(z) = \frac{aC_1}{k_B T}$. So,

$$(5.9) \quad p_1(z, \sigma) = \frac{-1}{I(z, \sigma)} \int \left(\left(\frac{aC_1}{k_B T} \right) \exp(\hat{r}(z)) \left(p_0(z, \sigma) \exp(-\hat{r}(z)) I(z, \sigma) \right)_z + \left(C_2 g'(2\pi\sigma) + 2\pi C_3 \sin(2\pi\kappa\sigma) \right) A_0(z) + \alpha_2 \left(\hat{\beta}(z) - \hat{\alpha}(z) \right) A_0(z) I_0 \left(\frac{aC_1}{k_B T} \right) I(z, \sigma) \right) d\sigma.$$

Since we are interested in the boundedness of p_1 we examine the following limit:

$$(5.10) \quad \begin{aligned} & \lim_{c \rightarrow \infty} \int_0^c \left(\exp(\hat{r}(z)) \left(p_0(z, \sigma) \exp(-\hat{r}(z)) I(z, \sigma) \right)_z + \left(C_2 g'(2\pi\sigma) + 2\pi C_3 \sin(2\pi\kappa\sigma) \right) A_0(z) + \alpha_2 \left(\hat{\beta}(z) - \hat{\alpha}(z) \right) A_0(z) I_0 \left(\frac{aC_1}{k_B T} \right) I(z, \sigma) \right) d\sigma \\ &= \lim_{c \rightarrow \infty} c \left(A_{0z}(z) - \hat{r}'(z) A_0(z) \right) + \alpha_2 \int_0^c \left(\hat{\beta}(z) - \hat{\alpha}(z) \right) A_0(z) I_0 \left(\frac{aC_1}{k_B T} \right) I(z, \sigma) d\sigma \\ & \quad + K(z, \sigma) \\ &= \lim_{N \rightarrow \infty} (N + \xi) \left(A_{0z}(z) - \hat{r}'(z) A_0(z) \right) + \alpha_2 \left(\hat{\beta}(z) - \hat{\alpha}(z) \right) A_0(z) I_0 \left(\frac{aC_1}{k_B T} \right) \\ & \quad \times \int_0^{N+\xi} I(z, \sigma) d\sigma + K(z, \sigma) \\ &= \lim_{N \rightarrow \infty} N \left(A_{0z}(z) - \hat{r}'(z) A_0(z) \right) + \alpha_2 N \left(\hat{\beta}(z) - \hat{\alpha}(z) \right) A_0(z) I_0^2 \left(\frac{aC_1}{k_B T} \right) \\ & \quad + K(z, \sigma) + O(\xi), \end{aligned}$$

where $K(z, \sigma) = (C_2 g(2\pi\sigma) - C_3 \cos(2\pi\kappa\sigma)) A_0(z) + K_1(z)$ is a bounded term. Also we have decomposed $c = N + \xi$ with $N = \lfloor c \rfloor$ and $0 \leq \xi < 1$.

Immediately, we see that in order to bound the $p_1(y, \sigma)$ solution we must take care of the unbounded part of the above limit. We do so by setting

$$(5.11) \quad -\hat{r}'(z) A_0(z) + A_{0z}(z) + \alpha_2 \left(\hat{\beta}(z) - \hat{\alpha}(z) \right) A_0(z) I_0^2 \left(\frac{aC_1}{k_B T} \right) = 0,$$

which gives us the following condition on the coefficient $A_0(z)$:

$$(5.12) \quad A_0(z) = \exp \left(\hat{r}(z) - \alpha_2 I_0^2 \left(\frac{aC_1}{k_B T} \right) \int \left(\hat{\beta}(z) - \hat{\alpha}(z) \right) dz \right).$$

Notice the striking similarity of this expression with the expression we derived for the in-register well in (4.13). In contrast to (4.13), for the expression of (5.12) the solution is greatly simplified due to the modified Bessel function, I_0 , being evaluated at the specific value $\frac{aC_1}{k_B T}$. This results in a constant coefficient multiplying the jump term expansion in the zero order solution in (5.12).

We can now write our approximation for the off-register case as

$$(5.13) \quad p_0(z, \sigma) = \exp \left(\frac{aC_1 \sin(2\pi\kappa\sigma)}{k_B T} + \hat{r}(z) - \alpha_2 I_0^2 \left(\frac{aC_1}{k_B T} \right) \int \left(\hat{\beta}(z) - \hat{\alpha}(z) \right) dz \right) + O(\varepsilon).$$

Next, we calculate the approximation for motor velocities using p_0 to obtain

(5.14)

$$\begin{aligned} v &\approx \delta \int_0^L (\alpha(x) - \beta(x)) p_0(x) dx + O(\varepsilon) \\ &= \delta C \int_0^L (\alpha(x) - \beta(x)) \\ &\quad \times \exp\left(\frac{aC_1}{k_B T} \sin\left(\frac{2\pi x}{s}\right) + \frac{r(x)}{k_B T} - \frac{\delta\nu}{k_B T} I_0^2\left(\frac{aC_1}{k_B T}\right) \int (\beta(x) - \alpha(x)) dx\right) dx \\ &\quad + O(\varepsilon). \end{aligned}$$

We can further simplify our analytic solution for the velocity by applying averaging for the velocity expression, which gives

(5.15)

$$\begin{aligned} v &\approx \delta \int (\alpha(z) - \beta(z)) \overline{p_0(z, \sigma)} dz + O(\varepsilon) \\ &= \delta C \int_0^L (\alpha(x) - \beta(x)) \exp\left(\frac{r(x)}{k_B T} - \frac{\delta\nu}{k_B T} I_0^2\left(\frac{aC_1}{k_B T}\right) \int (\beta(x) - \alpha(x)) dx\right) \\ &\quad \times I_0\left(\frac{aC_1}{k_B T}\right) dx + O(\varepsilon). \end{aligned}$$

A comparison between the expression obtained for p_0 in (5.13) and the numerical results from the previous section is shown in Figure 5.4.

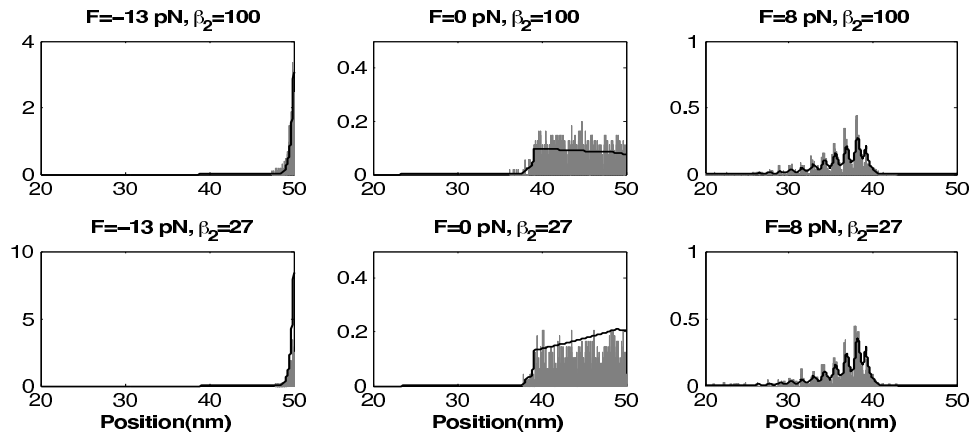


FIG. 5.4. Off-register well comparison of the numerical versus the analytical steady state distributions for the diffusive approximation of the steady state probability density function for varying loads F and $k = 0.001$.

Similar to the previous homogenization results from Figure 5.4, we see that the analytical expression for the steady state solution is in good agreement with numerical results. The main difference for $p_0(x)$ here as compared to the in-register calculation is that the value of k does not affect the approximate steady state distributions (recall that in (4.15), the term $I_0^2\left(\frac{f(x)}{k_B T}\right)$ depends on the value of the parameter k). Indeed, the independence of p_0 on k is a necessary feature due to the fact that the numerical

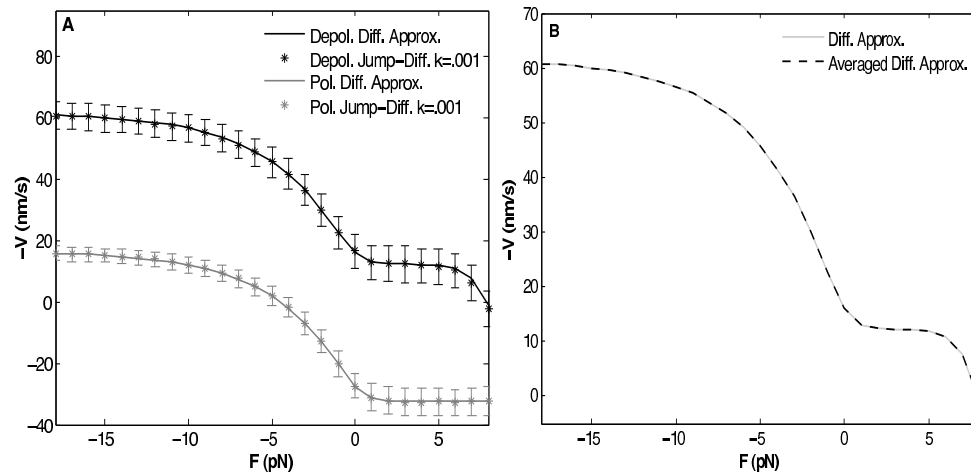


FIG. 5.5. (A) Off-register well load-velocity relationship comparison between the diffusive approximation $v_0(x)$ and the Monte Carlo simulations for $k = 0.001$ for a depolymerizing and a polymerizing motor of the off-register well. For the numerical simulations, bars represent standard deviations from the mean. (B) Load-velocity relationship comparison between the diffusive approximation load-velocity relationship as given in (5.14) and the averaged velocity in (5.15).

solutions of the steady state distributions show no changes as k is varied. Further, this also means that the analytical solutions presented here are a good match to the numerics for all the k values we have examined in this paper (for clarity, a comparison only for $k = 0.001$ is shown in Figure 5.4).

In Figure 5.5(A) we show a comparison between the numerical results for the force-velocity relation and our analytic solution from (5.14) (only the numerical solution for $k = 0.001$ is shown for clarity). The analytical velocity solution is a very good approximation of the numerical solutions for all the values of k we have considered. Similarly, a comparison between the averaged solution in (5.15) and the solution in (5.14) in Figure 5.5(B) shows that the averaged solution is in good agreement with the asymptotic solution and is thus an excellent fast approximation for the force-velocity relation.

In summary, in this section we have calculated analytical expressions for the force-velocity relation for the off-register motor. The solutions obtained are much simpler than the solutions for the in-register well. A distinguishing characteristic in the off-register well case is that the unit barrier amplitudes do not affect the analytic and numeric solutions as opposed to the in-register case, where the value of k significantly affects motor behavior. Therefore, the analytic solutions we obtained in this section are not only strikingly simple but also useful for a much wider range of parameters than in the in-register well case.

6. Conclusions. Understanding the mechanisms underlying the attachment of chromosomes to MTs presents various challenges due to the dynamic nature of the attached MTs. Even though many components of this attachment site have been identified there is no clear understanding of how these components combine with one another to create a motor that can robustly pull significant loads with velocities that depend on the rates of the attached MT tip.

In this paper we have proposed a mathematical model for Kt motors. Within our model framework, we can study the effect of the strength of Kt-MT binding on motor

velocities as well as the effects of variations in the polymerization/depolymerization rates of the attached kMT. We have also explored two cases for the model: (a) the in-register case in which the Kt binder period is an integer multiple of the MT binding site spacing, and (b) the off-register case in which the binder period is not an integer multiple of binding site spacing. In the in-register scenario we saw that for weak binding with low activation barriers the Kt model can be reduced to a simple model where closed form expressions for the velocity-force relationship can be obtained. We observed two modes for motor movement: (1) a slippery mode in which less load could be sustained (however, the motor moved with velocities that obeyed the balance of kMT rates), and (2) a sticky mode in which the motor becomes almost static (however, the threshold for breaking loads increases). In the slippery mode, motors act with velocities which are mostly insensitive to loads, since load variation for this motor results in coupler repositioning on the MT lattice, which preserves constant velocities as long as the new equilibrium position allows for the net rate of polymerization/depolymerization to remain constant. We also showed that variations in the kMT depolymerization rate for low unit activation in binding produce shifts in the force-velocity relationship which, depending on the balance of rates, can lead to a direction change for the motor due to chemical rate variations. This last feature is particularly important for our motor in the larger chromosome movement context.

In the off-register case we saw many of the characteristics observed for the in-register well. The main difference in this model scenario is the motor's reaction to variations in the unit activation barrier. Whereas the in-register case penalized the increased overlap between the coupler and the polymer, the off-register case penalty in free energy is much smaller. As a result, in the off-register case the motor only displays the slippery mode with no slow down as the unit activation barrier energy increases. This finding pointed us to the scenario that if the linkers are not highly organized, there could be an advantage in motor velocities since slow down would require high amounts of energy. Another advantage of the off-register well model is that analytic solutions can be obtained and result in surprisingly simple expressions that produce very good approximations for all the values of the unit activation barriers explored. The analytical approach is extremely valuable for this model for both the in-register and the off-register case since numerical simulations are time consuming. Given the current biological data, it is unclear which linker distribution case is operating at the Kt-MT interface. However, if the linkers are not organized into a higher order structure that would impose the same period for the binders as the MT lattice, we suspect that the off-register motor case would be a more appropriate Kt motor model. In this last scenario, we predict that changes in the Kt binding strength to kMTs caused by the phosphorylation of Ndc80 by Aurora B kinase would have to involve a large energy exchange in order to cause a Kt motor to stall.

Furthermore, in our study we also incorporated polymerization ratchet effects that arise from polymer pushing on the Kt plate. We saw that such effects are important when predicting the motility of Kts especially when the motor is subject to large pushing forces.

In conclusion, biased diffusion mechanisms coupled with spatial variations in kMT trip rates produce force-velocity relations which are distinctively nonlinear and are directly dependent upon Kt binding affinities to the MT lattice and the balance of kMT growth/shortening rates. Our Kt motor model is another example of a motility mechanism fueled by the chemical energy of polymerization coupled with the energy of polymer lattice binding to bias thermal motion in order to generate motion.

REFERENCES

- [1] I. M. CHEESEMAN AND A. DESAI, *Molecular architecture of the kinetochore-microtubule interface*, Nat. Rev. Mol. Cell Biol., 9 (2008), pp. 33–46.
- [2] C. CIFERRI, A. MUSACCHIO, AND A. PETROVIC, *The Ndc80 complex: Hub of kinetochore activity*, FEBS Lett., 581 (2007), pp. 2862–2869.
- [3] C. W. GARDINER, *Handbook of Stochastic Methods for Physics, Chemistry and the Natural Sciences*, 3rd ed., Springer Ser. Synergetics 13, Springer-Verlag, Berlin, 2004.
- [4] E. L. GRISHCHUK AND J. R. MCINTOSH, *Microtubule depolymerization can drive poleward chromosome motion in fission yeast*, EMBO J., 25 (2006), pp. 4888–4896.
- [5] T. L. HILL, *Theoretical problems related to the attachment of microtubules to kinetochores*, Proc. Natl. Acad. Sci. USA, 82 (1985), pp. 4404–4408.
- [6] A. P. JOGLEKAR AND A. J. HUNT, *Simple mechanistic model for directional instability during mitotic chromosome movement*, Biophys. J., 83 (2002), pp. 42–58.
- [7] A. P. JOGLEKAR, K. S. BLOOM, AND E. D. SALMON, *Mechanisms of force generation by end-on kinetochore-microtubule attachments*, Curr. Opin. Cell Biol., 22 (2009), pp. 1–11.
- [8] J. P. KEENER, *Principles of Applied Mathematics: Transformation and Approximation*, Perseus Books, Advanced Book Program, Cambridge, MA, 2000.
- [9] J. R. MCINTOSH, E. L. GRISHCHUK, M. K. MORPHEW, A. K. EFREMOV, K. ZHUDENKOV, V. A. VOLKOV, I. M. CHEESEMAN, A. DESAI, D. N. MASTRONARDE, AND F. I. ATAULLAKHANOV, *Fibrils connect microtubule tips with kinetochores: A mechanism to couple tubulin dynamics to chromosome motion*, Cell, 135 (2008), pp. 322–333.
- [10] T. J. MITCHISON AND E. D. SALMON, *Poleward kinetochore fiber movement occurs during both metaphase and anaphase-A in newt lung cell mitosis*, J. Cell Biol., 119 (1992), pp. 569–582.
- [11] I. M. MOLODTSOV, E. L. GRISCHCHUK, A. K. EFREMOV, J. R. MCINTOSH, AND F. I. ATAULLAKHANOV, *Force production by depolymerizing microtubules: A theoretical study*, Proc. Natl. Acad. Sci. USA, 102 (2005), pp. 4353–4358.
- [12] R. NICKLAS, *The forces that move chromosomes in mitosis*, Annu. Rev. Biophys. Biophys. Chem., 17 (1988), pp. 431–449.
- [13] C. S. PESKIN, G. M. ODELL, AND G. F. OSTER, *Cellular motions and thermal fluctuations: The Brownian ratchet*, Biophys. J., 65 (1993), pp. 316–324.
- [14] A. F. POWERS, A. D. FRANCK, D. R. GESTAUT, J. COOPER, B. GRACYZK, R. R. WEI, L. WORDEMAN, T. N. DAVIS, AND C. L. ASBURY, *The Ndc80 kinetochore complex forms load-bearing attachments to dynamic microtubule tips via biased diffusion*, Cell, 136 (2009), pp. 865–875.
- [15] B. SHTYLLA AND J. P. KEENER, *A mechanomolecular model for the movement of chromosomes during mitosis driven by a minimal kinetochore bicyclic cascade*, J. Theoret. Biol., 263 (2010), pp. 455–70.
- [16] R. V. SKIBBENS, V. PETRIE-SKEEN, AND E. D. SALMON, *Directional instability of kinetochore motility during chromosome congression and segregation in mitotic newt lung cells: A push pull mechanism*, J. Cell Biol., 122 (1993), pp. 859–875.
- [17] L. WORDEMAN AND J. R. COOPER, *The diffusive interaction of microtubule binding proteins*, Curr. Opin. Cell Biol., 21 (2009), pp. 68–73.